J Appl Electrochem (2010) 40:1337–1347
DOI 10.1007/s10800-010-0091-0

ORIGINAL PAPER

Photoactive WO_3 and Se-WO_3 thin films for photoelectrochemical oxidation of organic compounds

Simona Ostachaviciute · Jonas Baltrušaitis · Eugenijus Valatka

Received: 31 August 2009 / Accepted: 17 January 2010 / Published online: 29 January 2010

Abstract Thin films of bare and Se-containing tungsten trioxide (WO_3) on AISI304-type stainless steel were prepared by electrochemical deposition using peroxy-tungstate solutions. The obtained films were characterized by X-ray diffraction, photoelectron spectroscopy, scanning electron microscopy, thermal and photovoltammetry analyses. The oxidation of methylene blue, phenol, and methanol was used to evaluate the photoelectrocatalytic activity of the prepared films. It has been established that the incident photon-to-current efficiency (IPCE) in 0.1-M K_2SO_4 decreases as the concentration of methylene blue and phenol increases. On the contrary, the IPCE values increase with the increase in initial concentration of methanol. The bulk electrolysis experiments revealed that the prepared films are stable and can be used for photoelectrochemical oxidation of methanol.

Keywords Stainless steel · Mixed tungsten trioxide-selenium film · Electrodeposition · Photoelectrochemical oxidation

1 Introduction

Research on heterogeneous photo(electro)catalysis continues to attract attention among scientists throughout the world. It has been shown in numerous papers that nanocrystalline TiO_2 in anatase form appears to be the most suitable material for the oxidation of organic pollutants in water and air [1–8] or water photosplitting [9–11]. However, it still cannot be widely used in practical applications due to its sensitivity to primarily UV range of the spectrum and a fast recombination of photogenerated charge carriers. Thus, there is still a need for the photosensitive materials with improved spectral response spanning toward the visible region while maintaining a good stability. Moreover, it is necessary to find a suitable substrate for the immobilization of the photocatalysts, as the use of the suspensions is related with additional economic expenses for the catalyst separation.

Tungsten trioxide (WO_3) was the first semiconductor with a band gap smaller than that of TiO_2, which was shown to photoelectrolyze water and to be stable in acidic solutions [12]. WO_3 is an important electrochromic material which can be deposited on various substrates by electrochemical, sol–gel, sputtering, spray-pyrolysis, evaporation, and chemical vapor deposition methods [13]. In order to increase its efficiency in photocatalytic processes, WO_3 can be deposited on electroconductive substrates and biased positively by applying external voltage. In this way, the rate of photoelectron–hole recombination is reduced and the rate of surface redox reactions is increased. For synthesis of such electrodes, an electrochemical method could be a cost-competitive option [14, 15]. The electrochemical synthesis presents number of advantages, namely, possibility of the oxide film growth at low temperatures on electroconductive substrates of any shape, film properties can be tailored by varying bath composition and applied voltage and simplicity of synthesis equipment.

Hepel et al. showed [16–18] that nanocrystalline WO_3 films on a Pt mesh exhibit a higher photoelectrocatalytic

S. Ostachaviciute · E. Valatka (✉)
Department of Physical Chemistry, Kaunas University of Technology, Radvilenu pl. 19, 50254 Kaunas, Lithuania
e-mail: evalatka@ktu.lt

J. Baltrušaitis
Department of Chemistry and Central Microscopy Research Facility, 76 EMRB, University of Iowa, Iowa City, IA 52242, USA

activity than that of TiO_2 nanoparticulate electrode. Such WO_3 photoanodes were successfully employed for the mineralization of textile diazo dye pollutants (Naphtol Blue Black, Remazol Black B). Electrodeposited WO_3 films on IrO_2-coated Ti substrate can be used for efficient anodic oxidation of phenol in wastewater [19]. These films possess high chemical and physical stability and their electrocatalytic activity towards phenol mineralization is nearly comparable to that of PbO_2 anode which is used in many practical applications. The results indicate a strong influence of substrate nature and electrolyte composition on the structure of the deposited semiconductor films.

Georgieva et al. [20–22] extensively studied photoelectrochemical activity of electrodeposited TiO_2/WO_3 coatings on stainless steel substrate. It was found that WO_3 enhances activity of TiO_2 under UV and visible irradiation, and bilayer TiO_2/WO_3 electrodes were more active that TiO_2 or WO_3 alone. It has also been reported that the photoelectrocatalytic activity of WO_3 films can be improved by doping with Ti^{4+} [23], Zn^{2+} [24], or simply optimizing the synthesis procedure [25].

The aim of current work is to obtain photoactive WO_3-based coatings on stainless steel and determine their photoelectrochemical activity towards oxidation of model organic compounds (methylene blue, phenol, and methanol). This paper is relevant to the development of photochemical methods for the oxidative destruction of organic pollutants.

2 Experimental

2.1 Preparation of WO_3 and Se-WO_3 electrodes

Bare and selenium-containing (denoted as WO_3 and Se-WO_3 throughout this paper) WO_3 coatings on stainless steel were prepared by electrochemical deposition using a standard three electrode cell. AISI 304 stainless steel plates of 0.5-mm thick were used as support. All solutions were prepared with doubly distilled water and analytical grade reagents. Both selenious acid (H_2SeO_3, >99.8% purity) and sodium tungstate ($Na_2WO_4{\cdot}2H_2O$, purity >99.7%) were obtained from Reachim (Russia) and used as received. The electrolyte itself was prepared according to the following procedure. First, sodium tungstate solution was mixed with hydrogen peroxide (H_2O_2, 30%, Lach-Ner, Czech Republic). Second, selenious and nitric acids (HNO_3, 65%, Penta, Czech Republic) were added to the solution containing tungsten(VI)-peroxo complex. Only freshly prepared solutions were used for the measurements. All solutions were not deaerated during the experimental runs. All measurements were carried out at an ambient temperature (291 K). The as-deposited samples were thermally treated under air atmosphere at 673 K for 1 h as one preliminary study showed [26] that WO_3 films prepared this way generate the highest photocurrents. In order to form WO_3 and Se-WO_3 films on stainless steel substrate, the deposition potential was varied from −0.2 to −0.5 V. The obtained results showed that the most uniform and stable films are obtained at −0.35 V, electrolysis duration being 20 min. Under these conditions, the amount of electrodeposited WO_3 is 1.3 ± 0.1 mg cm^{-2}. Assuming that the bulk density of WO_3 is 7.16 g cm^{-3}, the calculated average thickness of these coatings is about 1.8 μm.

Bare selenium films were prepared by electrodeposition at −0.35 V and 291 K using 0.01-M H_2SeO_3 + 0.3-M HNO_3 electrolyte.

2.2 Analytical techniques

The photoactivity of WO_3 and Se-WO_3 thin films was investigated using photovoltammetric methods. The electrochemical measurements in the dark and under UV irradiation were performed by computer-controlled *Autolab PGSTAT12* (Ecochemie, The Netherlands) potentiostat/galvanostat. The GPES® 4.9 software was used for the collection and treatment of the experimental data. A two-compartment photoelectrochemical quartz cell was employed. The electrolyte volume in each compartment was the same (100 mL). The anodic compartment contained the WO_3 or Se-WO_3 working electrode and Ag, AgCl, KCl(sat) reference electrode. Throughout the paper all potentials are referred to this electrode. The cathodic compartment housed a platinum wire (geometric area about 15 cm^2) as a counter electrode. 0.1-M K_2SO_4 (purity > 99%, Reachim, Russia) solution was used as a supporting electrolyte. The back side of the working electrode was insulated with the epoxy resin in order to eliminate its contribution to the dark current. The coated area of electrode was carefully positioned in the path of the UV irradiation. A General Electric F8W/BLB lamp was placed at a distance of 2 cm from the WO_3 or Se-WO_3 electrode and was used as an UV radiation source. The lamp emits mainly in the 315–400 nm range, the peak wavelength λ_{max} being at 366 nm. The average power density at 366 nm was determined to be 1.8 mW cm^{-2} [27].

The incident photon-to-current efficiency (IPCE) value of a photoelectrode was calculated using the following expression [22]:

$$\text{IPCE}\ (\%) = 100\frac{1240 j_{\text{ph}}}{\lambda P},$$

where j_{ph} is the photocurrent density in mA cm^{-2}, λ the wavelength of the incident light in nanometers (the value used in this study was 366 nm), P the incident light intensity in mW cm^{-2}.

The photoelectrocatalytic activity of the prepared films was tested by oxidation of the model organic compounds: methylene blue dye ($C_{16}H_{18}N_3SCl{\cdot}3H_2O$, purity > 99%,

Reachim, Russia), phenol (C_6H_5OH, purity > 99.5%, Lachema, Czech Republic), and methanol (CH_3OH, purity > 99.5%, Lachema, Czech Republic). The same experimental set-up and conditions (solution volume, electrodes, UV radiation source) were used in both photovoltammetry and photoelectrolysis experiments. The only difference was that during the photoelectrolysis experiments the solution was thoroughly stirred.

The X–ray powder diffraction (XRD) data were collected with *DRON-6* (Bourevestnik Inc., Russia) powder diffractometer with Bragg–Brentano geometry using Ni-filtered CuK_α radiation and graphite monochromator. The crystallite size D_{hkl} was calculated from the line broadening using the Scherrer's equation [28]:

$$D_{hkl} = \frac{k \cdot \lambda}{B_{hkl} \cdot \cos \Theta},$$

where λ is the wavelength of the CuK_α radiation (1.54056×10^{-10} m), θ the Bragg diffraction angle, B_{hkl} the full width at the half maximum intensity of the characteristic reflection peak ($2\theta = 24.3°$), and k a constant (the value used in this study was 0.94).

A custom-designed Kratos Axis Ultra X-ray photoelectron spectroscopy (XPS) system was used to determine the elemental composition of the WO_3 and Se-WO_3 thin films. The experimental set-up for reactions and analysis has been described in detail before [29]. Briefly, the surface analysis chamber is equipped with monochromatic radiation at 1486.6 eV from an aluminum K_α source using a 500 mm Rowland circle silicon single crystal monochromator. The X-ray gun was operated using a 15-mA emission current at an accelerating voltage of 15 kV. Low energy electrons were used for charge compensation to neutralize the sample. Survey scans were collected using the following instrument parameters: energy scan range of 1200 to −5 eV; pass energy of 160 eV; step size of 1 eV; dwell time of 200 ms; and an X-ray spot size of 700 × 300 μm. High-resolution spectra were acquired in the region of interest using the following experimental parameters: 20–40 eV energy window; pass energy of 20 eV; step size of 0.1 eV; and dwell time of 1000 ms. One sweep was used to acquire all the regions. The absolute energy scale was calibrated to the Cu $2p_{2/3}$ peak binding energy of 932.6 eV using an etched copper plate. All spectra were calibrated using C1s peak at 285.0 eV. A Shirley-type background was subtracted from each spectrum to account for inelastically scattered electrons that contribute to the broad background. CasaXPS software was used to process the XPS data [30]. Transmission corrected relative sensitivity factor (RSF) values from the Kratos library were used for elemental quantification. An error of ±0.2 eV is reported for all the peak binding energies.

All scanning electron microscopy (SEM) images were acquired using the Hitachi S-4800 scanning electron microscope operating at 2-kV accelerating voltage. Samples were imaged without any conductive coating.

Differential scanning calorimetry and thermogravimetry (DSC–TG) analysis was performed on a Netzsch STA 409 PC Luxx (Netzsch GmbH, Germany) simultaneous thermal analyzer. The heating was carried out in air, the rate of temperature increase was 15 K min^{-1}, and the temperature range from 303 to 773 K was used.

Chemical oxygen demand (COD) was measured by the dichromate reflux method [31] in order to evaluate quantitatively methanol mineralization.

3 Results and discussion

3.1 Voltammetric behavior of stainless steel in peroxy-tungstate electrolytes

The voltammetric behavior of a stainless steel electrode in 0.1-M Na_2WO_4 + 0.1-M H_2O_2 + 0.3-M HNO_3 electrolyte is shown in Fig 1. The increase in current was observed at potentials negative to 0.1 V when sweeping towards the negative potential from the initial potential of 0.38 V. This observation can be related to several processes, such as the reduction of peroxy-tungstates and free hydrogen peroxide, hydrogen evolution. These results are in agreement with earlier studies on the electrodeposition of tungsten oxide using tungsten(VI)-peroxocomplexes [32]. When the potential was reversed at −0.45 V and scanned towards the positive values, several anodic peaks were observed at the potentials above 0.9 V (the inset of Fig. 1a). These peaks can be mainly associated with the dissolution of the stainless steel. It has been shown that in this potential region the transpassive dissolution of stainless steels occurs due to the release of soluble Cr(VI) and Fe(III) species [33]. Similar electrochemical behavior of the stainless steel electrode was observed in peroxy-tungstate solution containing 0.01-M H_2SeO_3 (Fig. 1b). An additional anodic peak at about +0.8 V was observed (the inset of Fig. 1b) due to the presence of selenium.

It must be emphasized that various species can be formed in the electrolyte used in this study and can play an important role in the electrodeposition mechanism. It is known that the yellow tetraperoxotungstate ions $[W(O_2)_4]^{2-}$ are formed in mildly alkaline or acidic solutions (pH 5–9) by the addition of excess H_2O_2 to WO_4^{2-}solution [34]. Below pH 5 these are progressively converted into the dimmers of diperoxo species $[W_2O_{11}]^{2-}$ or $[W_2O_3(O_2)_4(H_2O)_2]^{2-}$ [34]. In dilute acidic solutions (0.1–1 M H^+) the rapid formation of the monomeric species (presumably, $[WO(O_2)_2(H_2O)_2]^{2-}$)

occurs [34]. Addition of the selenious acid to the tungstate solution may lead to the formation of selenotungstic heteropolyacid [35]. In addition, the selenious acid can be oxidized in the presence of hydrogen peroxide to selenic acid [36].

In order to form WO_3 and Se-WO_3 films on stainless steel substrate, the deposition potential was varied from −0.2 to −0.5 V. The obtained results showed that the most uniform and stable films were obtained at −0.35 V, electrolysis duration being 20 min. Thus, in all subsequent experiments, we used WO_3 and Se-WO_3 electrodes prepared under these conditions.

3.2 Structural characterization of WO_3 and Se-WO_3 electrodes

Differential scanning calorimetry (DSC) and thermogravimetric (TG) analyses were performed to determine the thermal stability of the prepared samples in air (Fig. 2). Two endothermic phenomena are observed in the

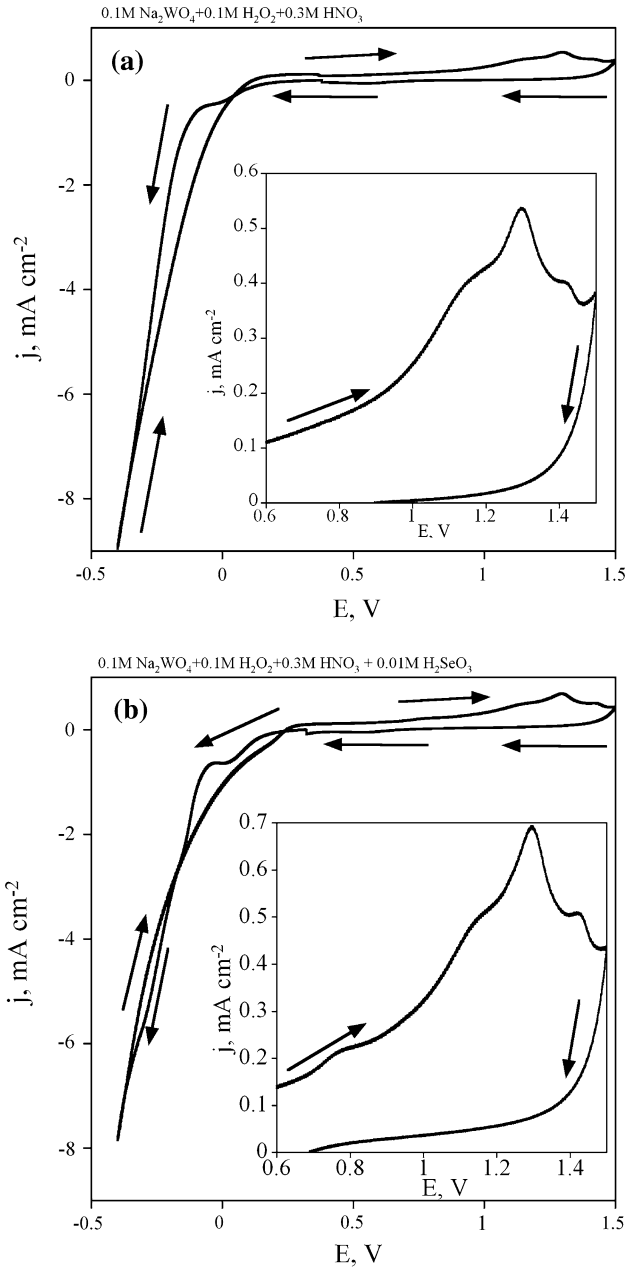

Fig. 1 Cyclic voltammograms of a stainless steel electrode in electrolytes of **a** 0.1-M Na_2WO_4 + 0.1-M H_2O_2 + 0.3-M HNO_3 and **b** 0.1-M Na_2WO_4 + 0.1-M H_2O_2 + 0.3-M HNO_3 + 0.01-M H_2SeO_3. Potential scan rate $\nu = 50$ mV s^{-1}

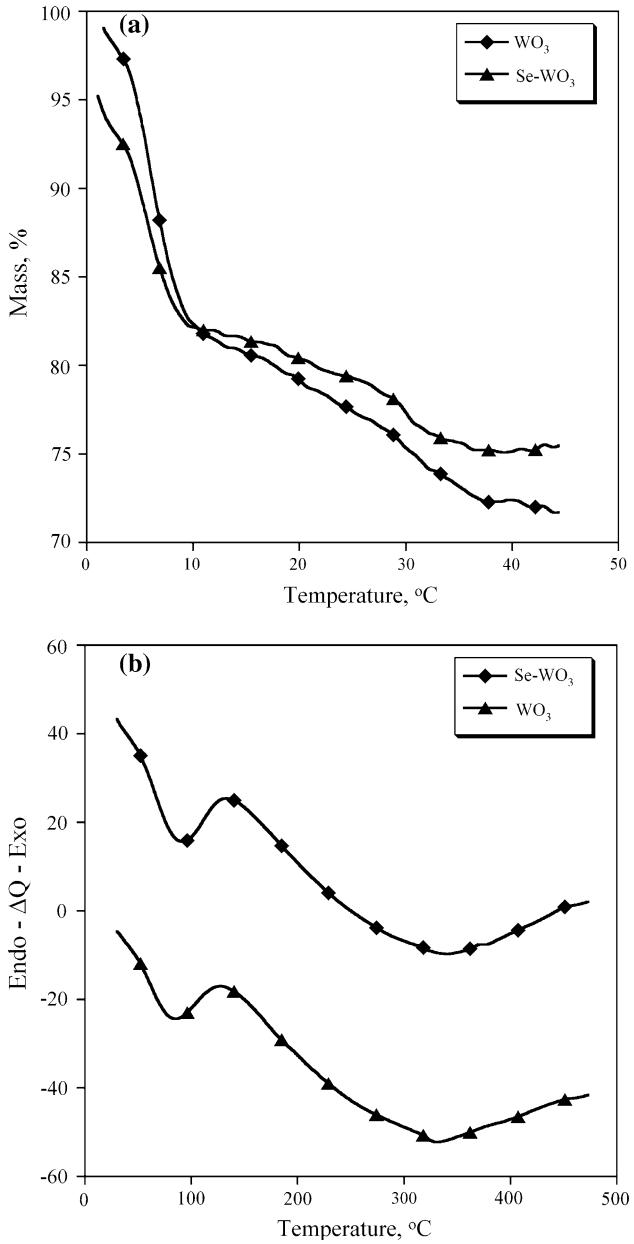

Fig. 2 TG (**a**) and DSC (**b**) patterns of as-deposited bare (denoted as WO_3) and Se-containing (denoted as Se-WO_3) tungsten oxides

temperature range of 303–673 K. They are accompanied by the weight loss of about 28% (bare tungsten oxide) and 25% (Se-containing tungsten oxide), respectively. The weight loss at 303–393 K can be related to the evaporation of physically adsorbed water molecules. The weight loss at higher temperatures (403–673 K) can be associated with the evaporation of chemisorbed water. It has been reported previously that electrochemical deposition leads to the formation of hydrated WO_3 containing various quantities of chemisorbed water, for instance, $WO_3 \cdot 0.5\ H_2O$, $WO_3 \cdot H_2O$ [19]. These results indicated a strong influence of the substrate nature and electrolyte composition on the structure of deposited semiconductor films.

XRD analysis of as-deposited samples showed only a halo at around 20°, thus suggesting an amorphous structure (Fig. 3). After the heat-treatment at 673 K for 1 h, the XRD analysis reveals diffraction peaks corresponding to the crystalline WO_3. According to the Scherrer's equation, the average WO_3 crystallite size was calculated to be 32.4 nm.

Chemical composition of the obtained WO_3 and Se-WO_3 films was characterized using XPS. High-resolution O1s, Se3d, and W4f spectra were obtained for WO_3, Se-WO_3, and bare Se films and are shown in Fig 4. No spectra are shown for the thin films that have no certain element (Se in WO_3 and W in Se film). The qualitative data for all films is summarized in Table 1. O1s spectra shown for all three films are composed of several components.

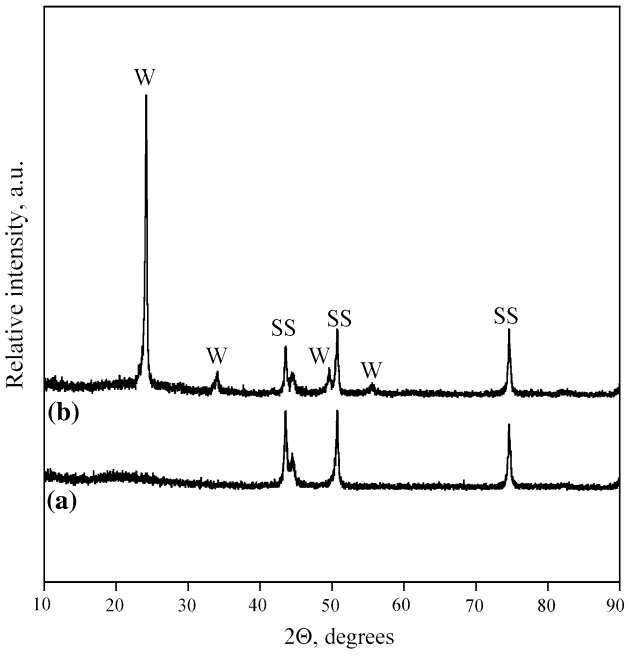

Fig. 3 XRD pattern of as-deposited (**a**) and annealed at 673 K (**b**) Se-WO_3 electrode. Indexes: *W* tungsten oxide, *SS* stainless steel

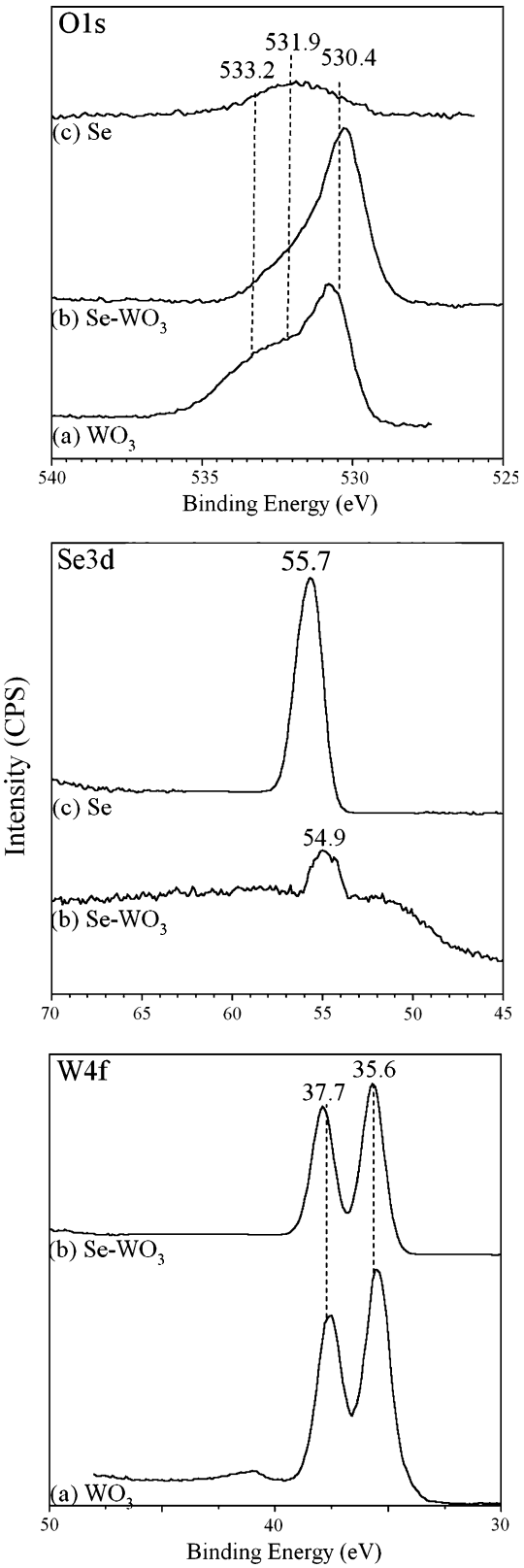

Fig. 4 High-resolution XPS spectra of O1s, Se3d, and W4f regions of representative WO_3, Se-WO_3, and Se films. Quantification data is shown in Table 1

Table 1 Results of XPS characterization of WO_3, Se-WO_3 and Se films deposited using 0.1-M Na_2WO_4 + 0.1-M H_2O_2 + 0.3-M HNO_3 + xH_2SeO_3, where x = 0.01, 0.005, 0.002, 0.001, and 0 M

Film	H_2SeO_3 concentration (M)	XPS composition (atomic%)		
		O1s	Se3d	W4f
WO_3	–	74.4	0.0	25.6
Se-WO_3	0.01	70.5	5.1	24.5
Se-WO_3	0.005	74.5	0.9	24.7
Se-WO_3	0.002	76.2	0.0	23.8
Se-WO_3	0.001	76.0	0.0	24.0
Se[a]	0.01	48.6	51.4	0.0

[a] Deposited using 0.3-M HNO_3 + 0.01-M H_2SeO_3 electrolyte at 291 K

Namely, peaks at 530.4, 531.9, and 533.2 eV can be observed, with former being a sharp peak in WO_3 and Se-WO_3. These can be attributed to the oxygen atoms in WO_3 [37, 38], surface hydroxyl groups, and adsorbed water [39], respectively.

Binding energies of oxygen atoms in WO_3 in O1s spectrum reported previously are very close to those reported here (530.4–530.8 eV [40, 41]), so W4f high-resolution spectra was acquired to unambiguously determine tungsten oxidation state. W4f spectra shown in Fig 4b show distinct $W4f_{7/2}$ and $W4f_{5/2}$ doublets with $W4f_{7/2}$ peak located at 35.6 eV. This is in a good agreement with previously reported values of 35.5 for WO_3, with that for WO_2 located at 32.5 eV [41]. Thus, WO_3 and Se-WO_3 films reported here have tungsten in 6+ oxidation state.

Finally, high-resolution Se3d doublet of bare selenium films is located at 55.7 eV, whereas that for Se-WO_3 film is at 54.9 eV. The shift in binding energy is due to the formation of tungsten bound selenium species, similar to those found in WSe_2 at 54.5 eV [42]. Peak at 55.7 eV in Se film is due to the elemental selenium and not to the SeO_2, which has been shown to be located at 58.85 eV [43]. On the basis of these results it can be inferred that the selenium is deposited predominantly in the form of selenide. However, more detailed structural and morphological characterizations are currently under investigation in order to clearly state the mechanisms of selenium incorporation into WO_3 and film nucleation.

XPS quantification data in Table 1 show that up to 5.1% of selenium was incorporated into the thin WO_3 films. No selenium was detected in Se-WO_3 films, when H_2SeO_3 concentration was lower than 0.005 M. This is due to the detection limit of the XPS (~0.5%) and a strong inelastically scattered W4f background, superimposed on Se3d peaks. In all WO_3 and Se-WO_3 films O1s/W4f ratio was ~3:1, corresponding to the empirical formula of WO_3. Bare selenium films, on the other hand, had an excess of oxygen on the surface with empirical formula of O1s/Se3d close to 1:1. This shows the presence of a thin (~3 nm) adsorbed hydroxide or mixed selenium-oxygen films formed during electrodeposition.

SEM images of the representative tungsten oxide, selenium and mixed selenium-tungsten films are shown in Fig. 5. Lower magnification images are shown in the left column, while finer film details can be seen in the right column. All films shown have distinct surface morphology. While WO_3 film consists of randomly positioned <50-nm particles in good agreement with XRD data (Fig. 5a, b), Se film is uniform with no distinct domains observed (Fig. 5e, f). Se-WO_3 film shown in Fig. 5c, d possesses morphological properties similar to those of WO_3 film shown in Fig. 5a, b. However, films are not continuous anymore and have small cylindrical holes, most likely originating from the gas evolution upon formation reaction.

3.3 Photoelectrochemical properties of WO_3 and Se-WO_3 thin films

3.3.1 Photoelectrochemical behavior in supporting electrolyte

The photoelectrochemical behavior of WO_3 and Se-WO_3 electrodes was determined from the current–potential curves obtained in 0.1-M K_2SO_4 solutions both in the dark and under UV irradiation (Fig. 6). The potential was swept from −0.2 to +1.0 V at 10 mV s^{-1}. The behavior of both electrodes is characteristic of the n-type semiconductor [44]. The observed anodic photocurrent can be related to the generation of hydroxyl radicals ($^{\bullet}OH$) and other oxidation products (e.g., H_2O_2) at the surface of WO_3 or Se-WO_3 electrodes [6]. The hydrogen peroxide is known to be formed as a result of the interaction of hydroxyl radicals. The presence of $^{\bullet}OH$ radicals on the surface of WO_3 under UV irradiation was earlier confirmed by radical-trapping technique [45].

For n-type semiconductor, the photocurrent is due to the diffusion or the migration of charge carriers, depending on whether semiconductor film is particulate or continuous, respectively. In a case of thick and continuous film, a depletion layer can be developed upon contact with electrolyte facilitating the separation of photogenerated holes and electrons. According to Gartner-Butler model [20], the presence of the depletion layer can be determined by plotting the square of the photocurrent density, j_{ph}^2, with respect to the applied potential, E. Figure 7 shows that the plots j_{ph}^2 versus E are linear in the rising parts of the photovoltammograms, thus, confirming the formation of the depletion layer in the prepared films.

The obtained results show that the Se-containing tungsten oxide electrode generates higher photocurrent than bare WO_3. For the latter, after the photocurrent onset at

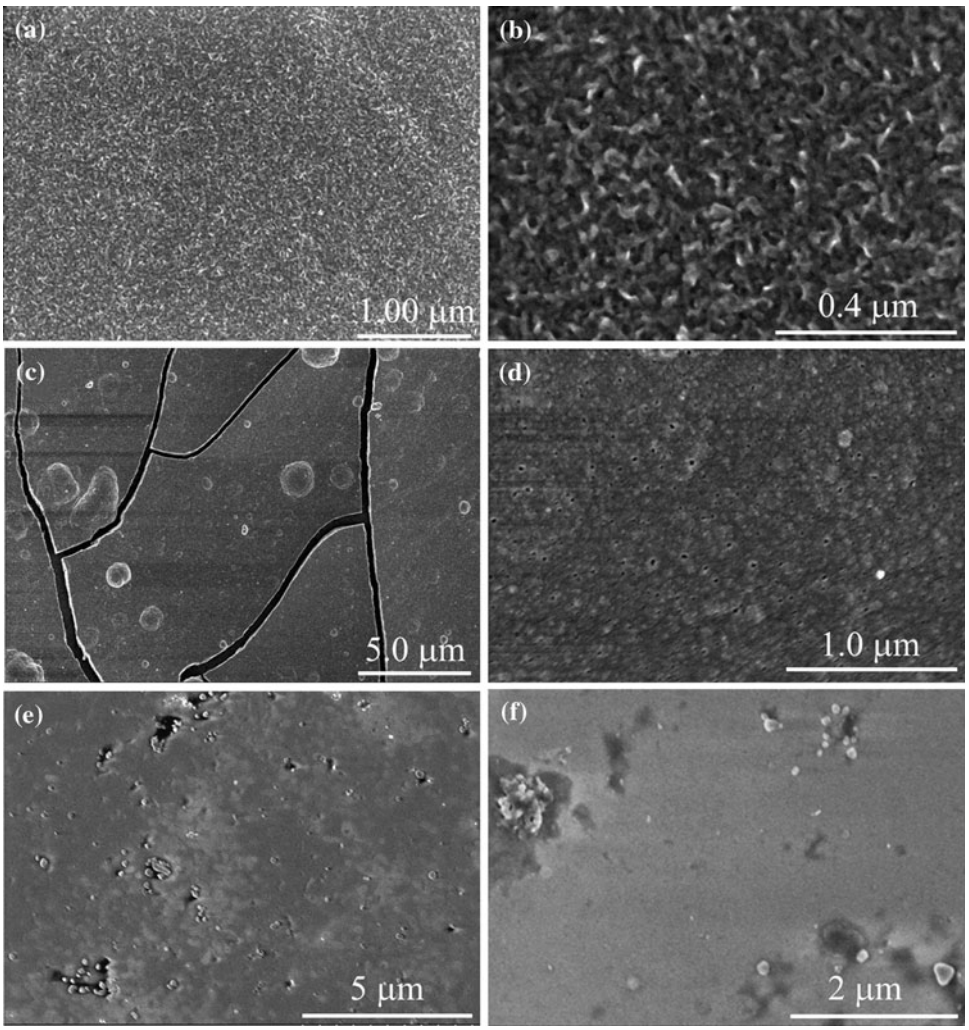

Fig. 5 Representative SEM images of WO_3 (**a**, **b**), Se-WO_3 (**c**, **d**), and Se (**e**, **f**) films. Lower magnification (*left*) and higher magnification (*right*) images are shown for each sample

about +0.23 V, a clear saturation of photocurrent is observed. The photocurrent onset potential for WO_3 and Se-WO_3 electrodes is more positive than those for TiO_2 film electrode due the higher flat-band potential [44].

On the basis of the photocurrent measurements, the IPCE values of both photoelectrodes were calculated and shown in Fig. 8a. It was found that these values are higher than those for Degussa P25 TiO_2 electrode measured under identical experimental conditions (2.88% at +0.6 V [27]).

3.3.2 *Photoelectrochemical behavior in the presence of organic compounds*

The obtained experimental data showed that the presence of methylene blue has negative effect on generation of the photocurrent. Consequently, the IPCE value decreased by increasing the amount of methylene blue in supporting electrolyte in the whole range of used concentrations (Fig. 8b). A similar dependence of photocurrent on initial solute concentration was observed in the case of phthalic and salicylic acids [46], which are known to be strongly adsorbed onto metal oxides. The authors suggested that the decrease in photocurrent can be related to the accumulation of aromatic intermediates at the electrode surface. These intermediates can act as photohole/photoelectron recombination centers and reduce the overall efficiency of the photocatalytic processes. It is known that various intermediate compounds are formed during methylene blue oxidation [47]. These compounds can interact differently with the oxide surface and markedly influence the processes of photohole capture. It has been established [48] that the initial step of MB photocatalytic oxidation is the cleavage of the bonds of the C–S+=C functional group leading to the formation of sulfoxide. The authors suggested that this step proceeds through an interaction with hydroxyl radicals, and photoholes are mainly involved in the decarboxylation reactions of MB oxidation intermediates. Carbon dioxide, nitrate, sulfate, and ammonium ions were also identified as reaction products, indicating that the complete oxidation of MB dye can be achieved; however,

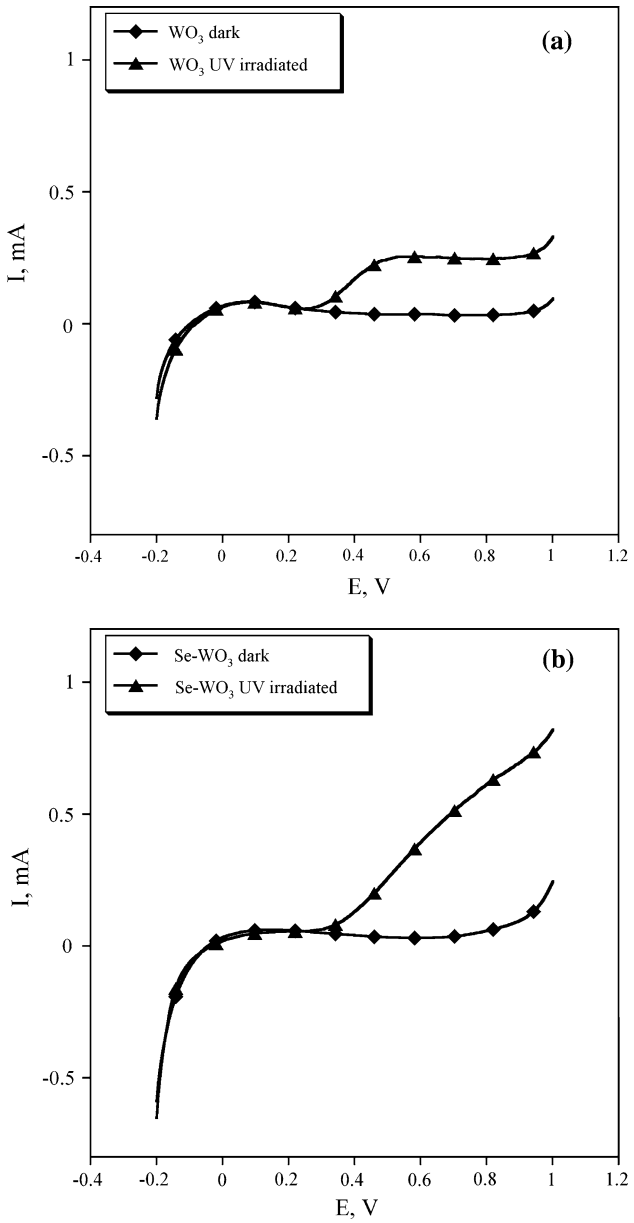

Fig. 6 Characteristic voltammograms in the dark and under UV illumination of **a** WO_3 and **b** Se-WO_3 electrodes annealed at 673 K. Potential scan rate $v = 10$ mV s^{-1}, 0.1-M K_2SO_4 solution at 291 K

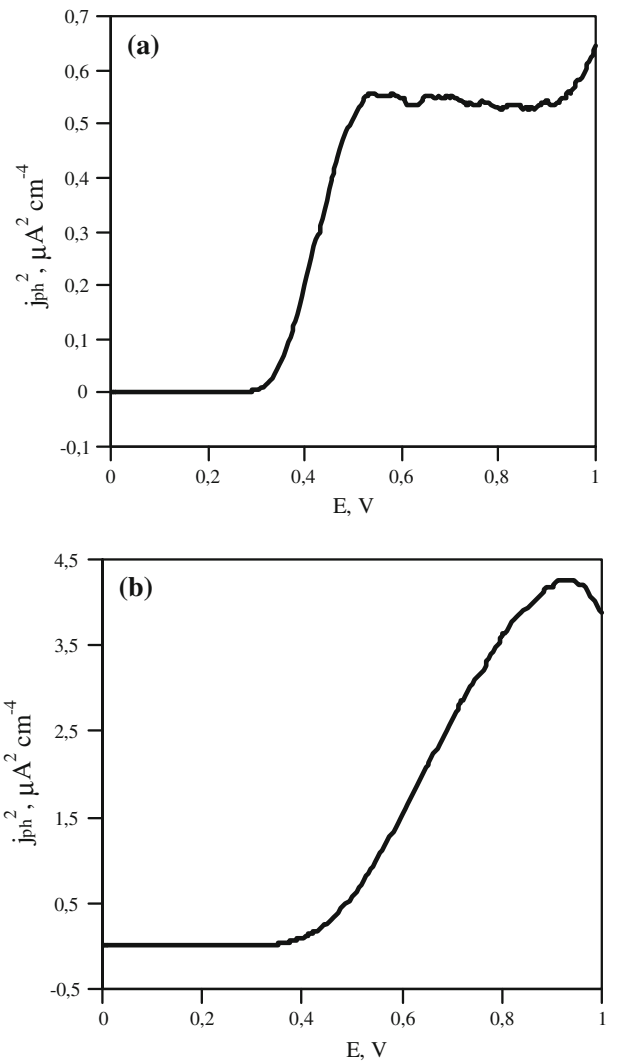

Fig. 7 Plots of the square of the photocurrent density, j_{ph}^2, with respect to the applied potential, E, for **a** WO_3 and **b** Se-WO_3 electrodes

the process is kinetically low. Moreover, the decrease in photocurrents can partly be attributed to UV light absorption by methylene blue molecules. For example, the molar absorption coefficient for MB at 366 nm was determined to be 1130 M^{-1} cm^{-1}. It means that 1-cm thick 1.4×10^{-5} M methylene blue solution absorbs at least 3.6% of incident UV irradiation.

It was determined that the small concentrations ($<1.10 \times 10^{-4}$ M) of phenol have no significant influence on the photocurrent. At higher concentrations the IPCE value decreased as in the case of methylene blue oxidation (Fig 8c). This effect can also be explained by the interaction of oxidation intermediate products with active centers on WO_3 surface. It has been established that the primary phenol degradation products are dihydroxy benzenes and quinones [49]. These products are further degraded upon time into low molecular carboxylic acids and finally to carbon dioxide and water.

Finally, the results in Fig. 8d show that the steady state photocurrent increases monotonically with methanol concentration. It has been stated [46] that the increase in observed photocurrent with substrate concentration suggests that the interaction of these compounds and their partially degraded intermediates with the oxide surface does not inhibit the photohole capture process. In order to establish the mechanism of photoelectrochemical oxidation of water dissolved pollutants, a kinetic model was

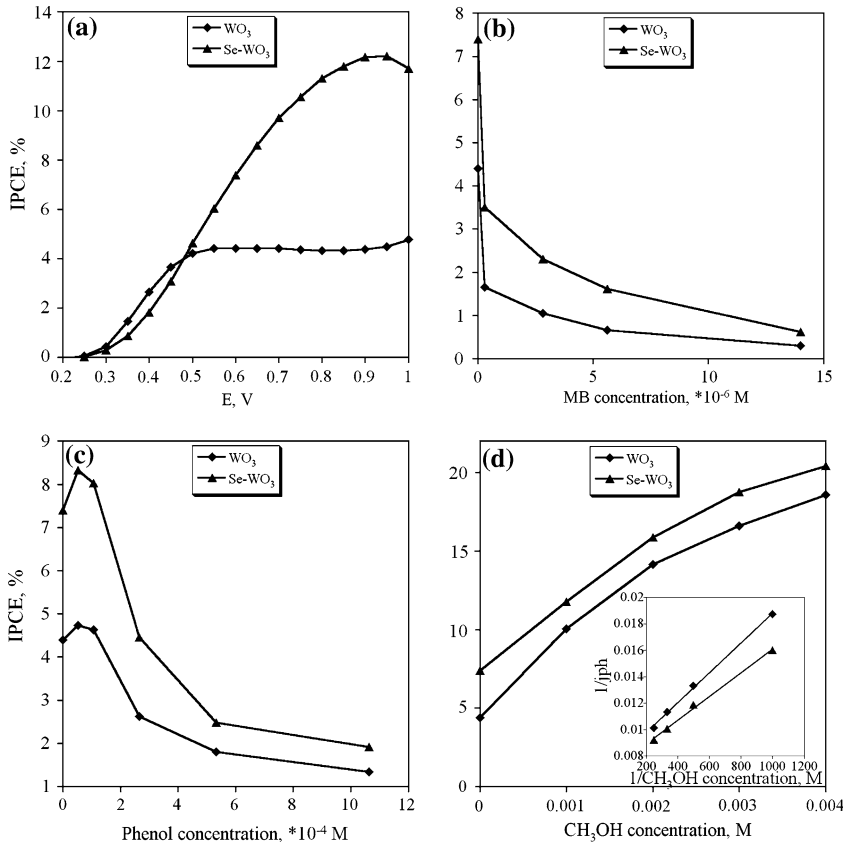

Fig. 8 The incident photon-to-current efficiency (IPCE) values for WO_3 and Se-WO_3 electrodes in 0.1-M K_2SO_4 electrolyte as a function of voltage bias (**a**) and the effect of initial concentration of methylene blue (**b**), phenol (**c**), and methanol (**d**) on IPCE values at +0.6 V. Inset in **d** dependence of $1/j_{ph} = 1/C_{CH_3OH}$ for the photoelectrochemical oxidation of methanol

developed [50]. It has been demonstrated that methanol oxidation mainly proceeds through an indirect hole transfer mechanism, via surface bound hydroxyl radicals, followed by the so-called current-doubling effect [51]. It is generally assumed [46, 50] that methanol molecules interact weakly with the oxide surface, they are not specifically adsorbed and do not compete with water molecules to be adsorbed on oxide surface. On the contrary, strong and specific adsorption seems to be a necessary condition for the direct hole mechanism, as is a case for formic acid [50].

Langmuir–Hinshelwood model is commonly used for the interpretation of the kinetic data in photocatalytic oxidation [6, 7]. In case of photoelectrochemical system, photocurrent density, j_{ph}, is proportional to the reaction rate and Langmuir–Hinshelwood model can be expressed as follows [20]:

$$j_{ph} = \frac{A'C^0}{C' + B'C^0},$$

where j_{ph} is photocurrent density, A', B', C' are constants, C^0 is initial solute concentration.

The inset of Fig. 8d shows the plot of $1/j_{ph} = f(1/C^0)$ for methanol. The obtained results confirm that the kinetics of the photoelectrochemical oxidation of methanol agrees well with Langmuir–Hinshelwood model.

3.3.3 *Methanol photoelectrolysis experiments*

The results of photoelectrochemical measurements provide very important information about kinetics of the oxidation processes. However, for practical applications the process efficiency must be known. For this purpose, a bulk oxidation of methanol in 0.1-M K_2SO_4 solution was performed using the prepared WO_3 and Se-WO_3 electrodes. Initial methanol concentration was 3×10^{-3} M. In order to evaluate the stability of the photoanodes, several consecutive experiments under the same conditions were carried out. Each experimental run lasted 2 h. The oxidation potential was kept constant at +0.6 V. No electrochemical oxidation of methanol was observed at this potential in the dark. Methanol mineralization degree X_m was estimated on the basis of COD measurements using the following equation:

$$X_m = \frac{COD_0 - COD_t}{COD_0} \cdot 100\%$$

where COD_0 and COD_t are values of COD in the beginning and after 2 h of reaction, respectively.

The obtained results are presented in Fig 9. They show only slight (2–4%) decrease in methanol mineralization rate for both electrodes during the first three experimental

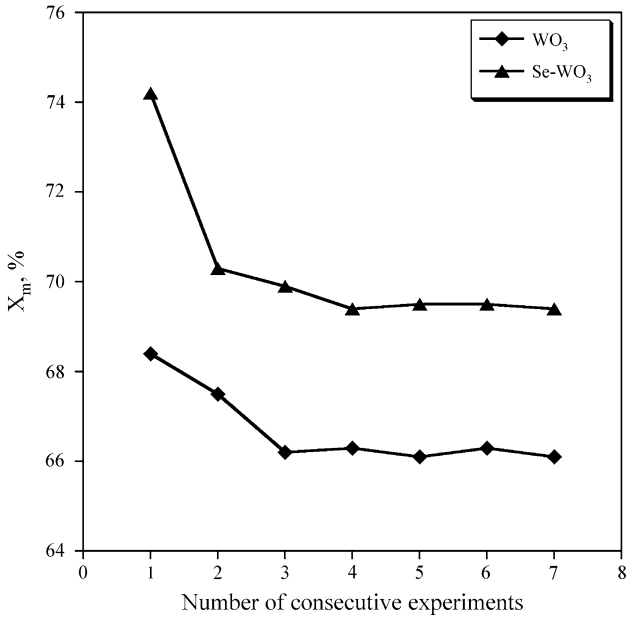

Fig. 9 Reusability of WO_3 and Se-WO_3 electrodes for photoelectrochemical mineralization of methanol at +0.6 V. *Lines* are added for the eye guidance only

runs. Later, the rate of electrochemical mineralization remained almost constant and the prepared electrodes showed a good photostability.

4 Conclusions

Thin films of WO_3 and Se-WO_3 on AISI304 stainless steel were prepared using the electrochemical deposition of peroxy-tungstate solutions. The as-deposited samples were thermally treated at 673 K in order to improve their crystallinity, photoactivity, and adsorption properties. It has been established that the presence of selenium enhances the IPCE for WO_3 photoanode in 0.1-M K_2SO_4 supporting electrolyte. Photoelectrochemical behavior of the prepared WO_3 and Se-WO_3 films in the presence of some model organic pollutants (methylene blue, phenol, methanol) was also investigated. It was determined that the IPCE decreases as the concentration of methylene blue and phenol increases. On the contrary, the IPCE values increase with increasing initial concentration of methanol. The obtained results show that the kinetics of the photoelectrochemical oxidation of methanol can be described in terms of Langmuir–Hinshelwood model. The bulk electrolysis experiments revealed that the prepared films are stable and can be used for photoelectrochemical oxidation of methanol.

Acknowledgments The authors gratefully acknowledge the Central Microscopy Research Facility (CMRF) at the University of Iowa and Kenneth Moore, Director of CMRF for access to the XPS and SEM.

References

1. Kabra K, Chaudhary R, Sawhney RL (2004) Ind Eng Chem Res 43:7683
2. Fujishima A, Zhang X (2006) C R Chim 9:750
3. Fujishima A, Rao TN, Tryk DA (2000) J Photochem Photobiol C 1:1
4. Bhatkhande D, Pangarkar VG, Beenackers AACM (2001) J Chem Technol Biotechnol 77:102
5. Peral J, Domenech X, Ollis DF (1997) J Chem Technol Biotechnol 70:117
6. Hoffmann MR, Martin ST, Choi W, Bahnemann DW (1995) Chem Rev 95:69
7. Linsebigler AL, Lu G, Yates JT Jr (1995) Chem Rev 95:735
8. Rodriguez JA, Fernandez-Garcia M (eds) (2007) Synthesis, properties, and applications of oxide nanomaterials. Wiley, New York
9. Ni M, Leung MKH, Leung DYC, Sumathy K (2006) Renew Sust Energy Rev 11:401
10. Nowotny J, Bak T, Nowotny MK, Sheppard LR (2007) Int J Hydrogen Energy 32:2609
11. Bak T, Nowotny J, Rekas M, Sorrell CC (2002) Int J Hydrogen Energy 27:991
12. Tomkiewicz M, Fay H (1979) Appl Phys 18:1
13. Granqvist CG (2000) Sol Energy Mater Sol Cells 60:201
14. Boccaccini AR, Zhitomirsky I (2002) Curr Opin Solid State Mater Sci 6:251
15. Therese GHA, Kamath PV (2000) Chem Mater 12:1195
16. Hepel M, Hazelton S (2005) Electrochim Acta 50:5278
17. Luo J, Hepel M (2001) Electrochim Acta 46:2913
18. Hepel M, Luo J (2001) Electrochim Acta 47:729
19. Habazaki H, Hayashi Y, Konno H (2002) Electrochim Acta 47:4181
20. Georgieva J, Armyanov S, Valova E et al (2005) J Electroanal Chem 585:35
21. Georgieva J, Armyanov S, Valova E et al (2006) Electrochim Acta 51:2076
22. Georgieva J, Armyanov S, Valova E et al (2007) Electrochem Commun 9:365
23. Radecka M, Sobas P, Wierzbicka M, Rekas M (2005) Physica B 364:85
24. Cheng XF, Leng WH, Liu DP et al (2007) Chemosphere 68:1976
25. Yagi M, Maruyama S, Sone K et al (2008) J Solid State Chem 181:175
26. Valatka E, Venskus A, Ancutiene I (2008) Chem Technol 2(48):30
27. Valatka E, Kulesius Z (2007) J Appl Electrochem 37:415
28. Azaroff LV (1968) Elements of X-ray crystallography. McGraw-Hill, New York
29. Baltrusaitis J, Usher CR, Grassian VH (2007) Phys Chem Chem Phys 9:3011
30. Fairley N (1999–2009) CasaXPS Version 2.3.14
31. Lur'e YY (1984) Analytical chemistry of industrial wastewater. Khimiya, Moscow (in Russian)
32. Meulenkamp EA (1997) J Electrochem Soc 144:1664
33. Betova I, Bojinov M, Laitinen T et al (2002) Corros Sci 44:2675
34. Dickman MH, Pope MT (1994) Chem Rev 94:569
35. Busev AI, Ivanov VM, Sokolova TA (1976) Analytical chemistry of elements: analytical chemistry of tungsten. Nauka, Moscow (in Russian)
36. Hughes FJ, Martin DS Jr (1955) J Phys Chem 59:410
37. Cantalini C, Wlodarski W, Li Y et al (2000) Sens Actuat B B64:182
38. Sivakumar R, Gopalakrishnan R, Jayachandran M, Sanjeeviraja C (2006) Smart Mater Struct 15:877

39. Tamboli D, Seal S, Desai V (2000) Mater Res Soc Symp Proc 566:89
40. Sarma DD, Rao CNR (1980) J Electron Spectrosc 20:25
41. Colton RJ, Guzman AM, Rabalais JW (1978) J Appl Phys 49:409
42. Guettari N, Ouerfelli J, Bernede JC et al (1998) Mater Chem Phys 52:83
43. Kazmerski LL, Jamjoum O, Ireland PJ et al (1981) J Vac Sci Technol 19:467
44. Grätzel M (1989) Heterogeneous photochemical electron transfer. CRC Press, Boca Raton
45. Leaustic A, Babonneau F, Livage J (1986) J Phys Chem 90:4193
46. Jiang D, Zhao H, Zhang S, John R (2006) J Photochem Photobiol A 177:253
47. Gnaser H, Savina MR, Calaway WF et al (2005) Int J Mass Spectrom 245:61
48. Houas A, Lachheb H, Ksibi M et al (2001) Appl Catal B 31:145
49. Berlan J, Trabelsi F, Delmas H et al (1994) Ultrason Sonochem 1:S97
50. Lana Villarreal T, Gomez R, Neumann-Spallart M et al (2004) J Phys Chem B 108:15172
51. Hykaway N, Sears WM, Morisaki H, Morrison SR (1986) J Phys Chem 90:6663